

**A Metal-on-Metal Growth Approach to Metal-Metal Oxide Core-Shell
Nanostructures with Plasmonic Properties**

Cameron C. Crane,[†] Ryan H. Manso,[†] Jun Li,[‡] Mourad Benamara,[§] Jing Tao,[‡] Yimei Zhu,[‡]
Feng Wang,[†] Jingyi Chen^{†,*}

[†]Department of Chemistry and Biochemistry, University of Arkansas, Fayetteville, AR
72701

[‡]Condensed Matter Physics and Materials Science Department, Brookhaven National
Laboratory, Upton, NY 11973

[§]Institute of Nanoscience and Engineering, University of Arkansas, Fayetteville, AR 72701

*Corresponding author: chenj@uark.edu (+1 479-575-6203)

Abstract: Hybrid core-shell nanoparticles integrate the material properties from individual components; however, the synthesis of core-shell nanoparticles with dissimilar materials remains challenging. In this work, we applied a metal-on-metal thin film growth approach to control the conformal deposition of nonprecious metal shells on the Cu-based metal cores to form core-shell structures of metal-metal oxide hybrids ($M-M'O_x$, where $M = AuCu_3$ or Cu , $M' = Fe, Mn, \text{ and } Ni$). The deposition kinetics were controlled by a temperature-regulated, thermal decomposition of zero-valent transition metal complexes. It is predicted that the conformal deposition can be promoted by keeping the initial deposition temperature close to the thermal decomposition temperature of the zero-valent precursors. The mechanisms of strain reduction and interdiffusion facilitate conformal deposition over island growth in the synthesis with slow reaction kinetics. This study provides insightful guidance to metal-on-metal growth in solution at the nanoscale and thus the seed-mediated approach to hybrid core-shell structures. The optical properties of these metal-metal oxide hybrids were investigated experimentally and interpreted by theoretical simulation. Despite damping effects, the plasmonic properties of these Cu-based core-metal oxide shell structures may have the potential to enable plasmon-enhanced applications.

Introduction

Composite nanostructures with two dissimilar materials have drawn considerable attention because they possess distinct properties from different materials in one entity and thus can potentially enable new uses of these materials in various applications. For example, plasmonic metal/semiconductor metal oxide composite materials can co-catalyze photochemical reactions,¹⁻² while coupling a plasmonic metal and a magnetic oxide can enable magnetoplasmonics for sensing and photonic devices.³⁻⁵ Magnetic oxides can also pair with catalytic metals to facilitate purification and catalyst recycling using magnetic separation.⁶⁻⁷ The optical and magnetic properties of the hybrid nanoparticles can be modulated through the control of the morphology and/or interface of dissimilar components *via* different synthetic strategies.^{5, 8-9} The synthetic methods to these hybrid materials can be categorized into two general approaches: seed-mediated growth and assembly of preformed nanoparticles. The former puts the two dissimilar components directly in contact with each other whereas the latter incorporates organic layers mediating the assembly of the adjacent nanoparticles.

The seed-mediated approach often relies on the heterogeneous epitaxial growth of the secondary dissimilar material on the primary seed material. One of the most commonly-used methods involves metal nanoparticles as seeds for the deposition of thermally-decomposed Fe atoms to form metal and metal oxide hybrid nanoparticles. Different configurations of the resulting hybrid nanoparticles were observed depending on their reaction conditions. For example, the dumbbell-like heterodimers of Fe₃O₄ and noble metals such as Au, Pt, and AuCu alloy were synthesized in nonpolar solvents.¹⁰⁻¹² By changing the polarity of the solvent, Au-Fe₃O₄ and Pt-Fe₂O₃ core-shell structures were formed.^{10, 13} More in-depth study on the reaction mechanism revealed that in addition to the solvent effect, different Fe precursors, [Fe]/[Au] ratios, surfactants, and reaction temperatures could affect the morphology of the products resulting in either dimers

or flower-like structures.¹⁴ Following the same trend, the mixture of dimers and flower-like Pd-Fe₃O₄ structures could be obtained through thermal annealing of the core-shell structures.¹⁵ Others found that the pallet shape of the metal seeds governed the epitaxial growth of iron oxide on the seed surface through the interfacial phase of metal-Fe alloys.¹⁶⁻¹⁷ These synthetic strategies were developed based on the noble metals as the seed materials due to their low chemical reactivity. Despite the latest heterostructured nanorod megalibrary built based on ion exchange reactions,¹⁸ employing reactive metals as seeds remains largely unexplored as a route towards metal-metal oxide core-shell nanostructures with plasmonic properties.

In this work, we applied a metal-on-metal growth approach to controllably synthesize the core-shell nanostructures of dissimilar materials using reactive Cu-based metals as cores and metal oxides as shells. The core-shell structures were achieved by controlling the temperature at which the metals, produced from thermally-decomposed precursors, deposit on the metal cores. The deposition process was demonstrated on the nanoparticle cores containing an earth abundant metal, Cu, including Cu-rich AuCu₃ nanorods and Cu nanoparticles. Three zero-valent metal precursors were used for the shelling process including iron(0) pentacarbonyl Fe(CO)₅, dimanganese(0) decacarbonyl Mn₂(CO)₁₀, and bis(1,5-cyclooctadiene)nickel(0) Ni(COD)₂. Upon exposure to oxygen after the deposition, the synthesis yielded core-shell nanostructures of AuCu₃-MO_x (M = Fe, Ni, and Mn) and Cu-MO_x (M = Fe, Ni, and Mn). The Cu cores of Cu-MO_x core-shell nanostructures were then removed through chemical etching with NH₄OH solution to generate hollow oxide nanoshells. Analogous to the well-established thin film growth, the mechanisms of the conformal deposition were discussed for the solution-based synthesis at the nanoscale. The optical properties of the resulting core-shell structures were measured experimentally using UV-vis spectroscopy and compared with the theoretical simulation to reveal the effects of oxide shells

on the plasmonic properties of the metals. The study provides mechanistic insight into the seed-mediated growth of dissimilar materials for the synthesis of hybrid metal-metal oxide core-shell and hollow metal oxide nanostructures. The optical properties of the hybrid core-shell structures may find potential use in various plasmon-enhanced applications.

Experimental Methods

Chemicals. Tetradecylamine (TDA, >95%) was purchased from T.C.I. Hydrogen tetrachloroaurate trihydrate ($\text{HAuCl}_4 \cdot 3\text{H}_2\text{O}$), 1-octadecene (ODE, 90%), $\text{Ni}(\text{COD})_2$, $\text{Mn}_2(\text{CO})_{10}$, ammonium hydroxide (NH_4OH , 28-30% NH_3 basis, 14.8 M), and copper 2,4-pentanedionate ($\text{Cu}(\text{acac})_2$) were purchased from Alfa Aesar. Oleylamine (OLAM, 70%) was purchased from Sigma-Aldrich. $\text{Fe}(\text{CO})_5$ was purchased from Acros Organics.

Synthesis of AuCu_3 nanorod seeds. The AuCu_3 nanorods were synthesized using our previously-reported procedure.¹⁹ Briefly, TDA (20 mmol, 4.30 g) and $\text{HAuCl}_4 \cdot 3\text{H}_2\text{O}$ (0.05 mmol, 19.7 mg) were added to a 25 mL three-neck flask equipped with a magnetic stir bar. Argon was flowed over the mixture for 10 min prior to heating and used as a protective gas throughout the reaction. The reaction mixture was heated to 160 °C and maintained at 160 °C for 20 min. Immediately after, $\text{Cu}(\text{acac})_2$ (0.2 mmol, 52.4 mg) in 1 mL of OLAM was injected to the reaction mixture, followed by heating the reaction to 210 °C and maintaining at 210 °C for another 20 min. After the reaction, the product was purified by adding toluene and centrifuging at 3900 rcf for 2 min to remove excess reactants and surfactants. At this step, the reaction mixture should remain above the melting point of TDA (40 °C) to avoid its solidification. The dispersion of the purified AuCu_3 nanorods in toluene exhibited a green color with the absorbance at ~650 nm.

Synthesis of $\text{AuCu}_3\text{-FeO}_x$ core-shell nanostructures. The deposition of Fe(0) from the thermal decomposition of $\text{Fe}(\text{CO})_5$ on the AuCu_3 nanorods was applied to synthesize $\text{AuCu}_3\text{-FeO}_x$ core-

shell nanostructures. In a typical procedure, AuCu₃ nanorods (5-6 mg) dispersed in toluene were added to a 25 mL three-neck reaction flask equipped with a magnetic stir bar, and the toluene was removed under an argon flow. The argon-dried nanorods were dispersed in 5 mL ODE and 0.2 mL OLAM *via* sonication. Argon was then flowed over the mixture for 20 min and used as a protective gas throughout the reaction. The temperature was raised to 110 °C and held at 110 °C for 10 min, followed by adding Fe(CO)₅ (0.148 mmol, 20 μL). Immediately after, the reaction mixture was heated at a rate of 2.5 °C/min to 200 °C for the deposition of a thin shell (1-2 nm) or to 280 °C for the deposition of a thick shell (5-6 nm). For both thin and thick shells, the reactions were held at these respective temperatures for another 60 min. After the reaction, the product was cooled to room temperature and purified by adding 25 mL of ethanol and centrifuging at 7800 rcf for 5 min, followed by dispersing in 20 mL toluene and 10 mL ethanol and centrifuging a second time at 3900 rcf to remove excess reactants, surfactants, and free iron oxide nanoparticles if any.

Synthesis of AuCu₃-NiO_x core-shell nanostructures. The FeO_x deposition method was modified by replacing Fe(CO)₅ with Ni(COD)₂ (0.148 mmol, 40 mg) dispersed in ODE.

Synthesis of AuCu₃-MnO_x core-shell structures. The FeO_x deposition method was modified by replacing Fe(CO)₅ with Mn₂(CO)₁₀ (0.148 mmol, 58 mg) dispersed in ODE.

Synthesis of Cu-MO_x (M = Fe, Ni, and Mn) core-shell nanostructures. The Cu nanoparticles were produced by reducing Cu(acac)₂ in the presence of OLAM, TOP and the *in situ* generated CO using our previously-reported procedure.²⁰ These Cu nanoparticles were used to replace the AuCu₃ nanorods in the deposition process to yield the Cu-MO_x core-shell nanostructures.

Synthesis of oxide hollow nanoshells. The oxide hollow nanoshells were obtained by etching the Cu cores in the Cu-MO_x core-shell nanostructures using NH₄OH solution. In a typical procedure, the Cu-MO_x core-shell nanostructures were precipitated from toluene by centrifugation and then

redispersed in ethanol, at which point, NH_4OH solution was added to reach 25 vol.%. The etching process was carried out in air overnight. After etching, the product was purified by centrifugation and resuspended in ethanol. The completion of the etching process was determined by a lack of blue Cu aqua-ammonium complex color when NH_4OH solution was added to the purified product.

Characterization. The transmission electron microscopy (TEM) images were captured using a transmission electron microscope (JEOL JEM-1011) with an accelerating voltage of 100 kV. High angle annular dark field scanning transmission electron microscopy (HAADF-STEM) images, high-resolution TEM (HRTEM) images, and energy-dispersive X-ray (EDX) mapping were obtained using a double Cs-corrected JEOL JEM-ARM200F microscope. X-ray powder diffraction (XRD) was performed using a bench-top x-ray diffractometer (Rigaku Miniflex II) equipped with Cu $K\alpha$ radiation source operated at 30 kV/15 mA. The concentrations of metals were determined using a flame atomic absorption (AA) spectrometer (GBC 932) and an inductively coupled plasma mass spectrometer (Thermo Scientific iCAP Q ICP-MS). X-ray photoelectron spectroscopy (XPS) was performed using PHI VersaProbe station. The XPS spectra were analyzed using CasaXPS Software. The UV-vis spectra were taken on a UV-vis spectrophotometer (Agilent Cary 50). The magnetic properties were measured by a superconducting quantum interference device (SQUID).

Simulation. The optical properties were calculated according to the discrete dipole approximation (DDA) using the DDSCAT 7.3 program.²¹⁻²² In this formalism, the structure is represented by an array of dipole moments residing within its volume. Each volume element is represented as a dielectric continuum with the complex dielectric response function of bulk materials. The complex dielectric response function of bulk AuCu_3 is assumed to be a linear combination of those of bulk Au and Cu.²³ The complex dielectric response function of bulk Fe_3O_4 is obtained from literature.²⁴

The optical cross sections were averaged over the two orthogonal polarization directions of the incident light. The optical efficiency, Q , is reported as the ratio of the respective optical cross section to $\pi \cdot a_{eff}^2$, where the effective radius, a_{eff} , is defined as the radius of a sphere with a volume identical to that of the structure of interest. The optical spectrum was simulated for each structure in toluene.

Results and Discussion:

A metal-on-metal growth approach that has been widely studied in thin film vapor deposition was applied to the deposition process of secondary metals on metal cores in solution yielding core-shell nanostructures. This approach can be viewed as an extension of the seed-mediated method. We demonstrated this approach using AuCu₃ nanorods as the cores for the deposition of oxygen-labile metal atoms obtained from the thermal deposition of zero-valent metal complexes such as Fe(CO)₅. Upon exposure to air, these core-shell nanostructures turned into metal-metal oxide hybrid core-shell nanostructures. The AuCu₃ cores were synthesized *via* our previously-published method,¹⁹ yielding a product consisting of 94% nanorods with a dimension measured to be 9.6×21.3 nm (diameter: 9.6 ± 1.3 nm; length: 21.3 ± 3.8 nm) and 6% spherical particles with a diameter of ~ 10 nm, as shown in Figure 1A. A fixed amount of these nanorods (0.5 mg) was used for the deposition of Fe shells at three different reaction temperatures, 200, 280, and 315 °C to yield FeO_x shells upon exposure to air after the reaction. We found that the reaction temperature had a strong influence on the deposition process and the aspect ratio of the AuCu₃ cores. At 200 °C, a uniform coating with a thickness of 1-2 nm was deposited on each nanorod to form a AuCu₃-FeO_x core-shell structure (Figure 1B). The sample consisted of 78% rod-shaped particles with a 9.0×20.4 nm core (diameter: 9.0 ± 0.9 nm; length: 20.4 ± 2.4 nm) and 22% spherical particles with a 10 nm core. When the reaction temperature increased to 280 °C, the shell thickness on individual

nanorods increased to 5-6 nm (Figure 1C). The sample consisted of 48% rod-shaped particles with a 9.6×18.3 nm core (diameter: 9.6 ± 1.0 nm; length: 18.3 ± 2.4 nm) and 52% spherical particles with a 10 nm core. Increasing the reaction temperature to 315 °C yielded a mixture of core-shell structures with a thin shell and an excess amount of free FeO_x nanoparticles (Figure 1D). Since the $\text{Fe}(\text{CO})_5$ decomposition rate and thus the amount of Fe atoms increases with the reaction temperature, the shell thickness increases with the deposition temperature until the critical temperature (285 – 288 °C) of $\text{Fe}(\text{CO})_5$.²⁵ Above the critical temperature where the density of liquid $\text{Fe}(\text{CO})_5$ and gas $\text{Fe}(\text{CO})_5$ is the same, the available Fe atoms for deposition in the reaction solution decreases because the excess Fe atoms could separate from the deposition solution in the gas phase and self-nucleate. As a result, the reaction yielded the core-shell structures with a thinner shell and free iron oxide particles as an unwanted by-product.

The conformal deposition of Fe on AuCu_3 to form core-shell structures at the nanoscale can be explained by its bulk counterpart of the ultrathin film epitaxial growth of Fe on Cu,²⁶⁻²⁹ Au,³⁰ or their alloy Cu_3Au .³¹⁻³⁵ Bauer's equilibrium criterion predicts the Volmer-Weber morphology (the island formation)³⁶ due to their small and often positive interfacial free energies; however, it is possible to deposit two-dimensional (2-D) films of the high-surface-free-energy metal Fe on the low-surface-free-energy metals such as Cu and Au. These metastable states of the 2-D film growth are favored over the three-dimension (3-D) island formation and can be attributed to the following two mechanisms: the balance between the strain energy and the surface-free-energy of the adsorbate-substrate,³⁵ and the intermixing of overlayer and substrate atoms.²⁹ To look into these mechanisms at the nanoscale, we further characterized the $\text{AuCu}_3\text{-FeO}_x$ core-shell nanostructures by HRTEM imaging, HAADF-STEM imaging, and EDX elemental mapping.

The HRTEM images of the core-shell nanostructures, as shown in Figure 2, A and D, reveal

that the ~2 nm thin shell appears to be less ordered with smaller crystalline domains compared to the ~5 nm thick shell. The XRD results confirm that the amorphous thin shell lacks observable FeO_x patterns but the more crystalline thick shell is indicated by the identifiable Fe_3O_4 pattern (Figure S1). The increased crystallinity for the thicker shell results from the higher reaction temperature used during the deposition process. As it can be seen, the thicker shell tends to deposit around the long side, or less curved surfaces, of the rods. This suggests that the strain energy at the interface increases with the increased crystallinity of the overlayer, resulting in the island growth rather than conformal deposition. The strain energy rises rapidly at the highly-curved surfaces, in this case both ends of the nanorods, where the cracks of the thicker, more crystalline shell occur. To minimize surface free energy, the island growth occurs to offset the rise of the strain energy due to the increased crystallinity and the high surface curvature, similar to the examples reported in literature for the formation of the hybrid dimer structures.^{10, 37-38} In other words, the conformal deposition on the cores can be facilitated by amorphous shells and small curvature cores.

The HAADF-STEM images of the core-shell nanorods with a thin shell and a thick shell, as shown in Figure 2, B and E, confirm the trend of conformal deposition and island growth observed in the HRTEM images. The EDX mapping shown in Figure 2, C and F, verifies the elemental distribution of an Fe and O-containing shell on the Au and Cu-containing core for both core-shell structures. The presence of Fe in the thin shell was further validated by the EDX spectral analysis of Figure 2C and the results were included in Figure S2. From these TEM results, it is impossible to tell whether there is intermixing between the overlayers and the cores. Instead, there appears to be a gap between the core and the shell in some of the core-shell nanostructures. This can be attributed to the following two factors: the etching of Cu from the AuCu_3 cores by OLAM³⁹ and

the nanoscale Kirkendall effect during the oxidation of Fe to FeO_x.⁴⁰⁻⁴¹ From the XRD results in Figure S1, the valence of the Fe in the core-shell structures with a thick shell is a mixture of 2+ and 3+ which is in agreement with our previous study of Pd-Fe₃O₄.¹⁵ The XPS analysis confirms the mixed 2+ and 3+ valence state of Fe for the thick shell (Figure S3A). The valence state of Fe in thin shell is mainly 2+ (Figure S3B).

These AuCu₃-FeO_x core-shell hybrid nanostructures are expected to exhibit both optical and magnetic properties stemming from each individual component. The AuCu₃ nanorods exhibit an extinction peak at 645 nm in the UV-vis spectrum (Figure 3A) that can be assigned to the longitudinal mode of its localized surface plasmon resonance (LSPR). Compared to the LSPR longitudinal mode of the pristine AuCu₃ nanorods, the peak shifts to the red at 710 nm with a shoulder at 573 nm appearing upon the deposition of a thin FeO_x shell (Figure 3B). Thickening the oxide shell, however, only results in a single peak at 590 nm (Figure 3C). In addition to the optical properties, these AuCu₃-FeO_x core-shell nanostructures possess magnetic properties. Figure 3D plots the magnetization of the two core-shell structures as a function of magnetic field strength. Although the iron oxide component is a shell, it acts as a single giant magnetic moment and appears superparamagnetic without hysteresis. The magnetization magnitude of the core-shell structures with a thick shell is higher than those with a thin shell due to the increased crystallinity resulting from the increased reaction temperature from 200 to 280 °C.⁴²

The LSPR peak characteristics are known to be sensitive to size, shape, and the surrounding medium of the nanoparticles.⁴³⁻⁴⁴ To understand the optical properties of the hybrid nanoparticles, we performed numerical simulations using the established DDA method.²¹⁻²² Figure 4A displays the simulated optical spectra of a AuCu₃ nanorod with an aspect ratio of 9.6 × 21.3 nm that is treated as an ellipsoid. For the aspect ratios studied, cylindrical targets and ellipsoidal targets gave

almost identical peak characteristics as shown in Figure S4. Ellipsoid targets were used to take advantage of the capacity of DDSCAT to create core-shell structures automatically. The simulated extinction spectrum shows the longitudinal mode of the LSPR located at 647 nm. Additional simulations of the nanorods with different aspect ratios at a fixed diameter of 10 nm indicate that both the position and optical efficiency of the longitudinal modes of the nanorods correlate linearly with their aspect ratios, as shown in Figure 4B. The linear fittings of the data were plotted in Figure S5. With a 10 nm diameter, one might anticipate the nanorods to exhibit a transverse mode at approximately 560 nm. However, such a mode is absent both in the measured and simulated spectrum. These simulated results agree well with the experimental data in Figure 3A and our previous study.¹⁹ The absence of the transverse mode at ~560 nm can be attributed to its relatively-low LSPR efficiency because the energy of the transverse mode overlaps the interband transition of Au and Cu materials, resulting in the damping of the LSPR. By moving away from the interband transition, the efficiency of the longitudinal mode drastically increases, with a more than six-fold enhancement (from 0.5 to 3.3) in the case of the nanorod with an aspect ratio of 1:2.2 (i.e., 9.6×21.3 nm or 10×22 nm). The significantly enhanced longitudinal mode efficiency thus overwhelms the transverse mode.

The simulation manifests that coating the AuCu₃ nanorod (Figure 4A) with a conformal Fe₃O₄ shell causes the longitudinal mode of the LSPR to shift to the red and decrease its efficiency, as shown in Figure 4C. The fittings of the data were plotted in Figure S6. The increase of thickness of the Fe₃O₄ shell leads to more significant redshifts of the longitudinal mode and more pronounced efficiency reduction. For shell thickness at or beyond 1.5 nm, the transverse mode starts to appear at around 600 nm as a shoulder. Since the thin shell AuCu₃-FeO_x core-shell sample in Figure 1B consists of 78% rod-shaped particles and 22% spherical particles, we simulated the

optical spectrum of this sample using a linear combination of both morphologies (a 9.6×21.3 nm rod and a 10 nm sphere of AuCu_3) with a thin Fe_3O_4 shell of 1.5 nm. The combined spectrum (Figure 4D) shows a main peak at 725 nm corresponding to the longitudinal mode of the rod-shaped particle and a shoulder at 600 nm corresponding to the contributions from the transverse mode of the rod-shaped particle and the LSPR of the spherical particle. This simulated result helps to interpret the two observed peaks in the optical spectrum of the core-shell structures with a thin shell as shown in Figure 3B. The main peak at 710 nm arises from the longitudinal mode of the rod-shaped core-shell particles with the shoulder at 573 nm from the transverse mode of the rod-shaped core-shell particles and the LSPR of the spherical core-shell particles.

For the sample with a thicker Fe_3O_4 shell, since the majority of the rod-shaped particles are only coated around the long sides of the nanorods with both ends exposed as shown in Figure 2D, we simulated the optical spectrum of the core-shell nanorod with both ends exposed and compared to that of the nanorod (a 9.6×18.3 nm rod of AuCu_3) with a uniform shell of 5 nm, as shown in Figure 4E. The uniform conformal core-shell nanorod exhibits two broad bands with the longitudinal mode at 760 nm and the transverse mode at 620 nm. Removing the coating from the two ends of the nanorod results in only one main peak at 620 nm and a very broad weak shoulder at 760 nm. In this case, the longitudinal mode is suppressed due to the damping effect of the Fe_3O_4 coating on the long sides of the rod, leading to the spectrum to be dominated by the transverse mode of the LSPR. Considering that the thick shell $\text{AuCu}_3\text{-FeO}_x$ core-shell sample (Figure 1C) consists of 48% rod-shaped particles and 52% spherical particles, we have to account for the contribution from the spherical particles to the optical spectrum of the sample shown in Figure 3C. Figure 4F displays the simulated spectrum (red dash curve) computed with a linear combination of the spectra of rod-shaped particles (blue curve in Figure 4E and 4F) and spherical particles

(black curve). The spherical particles have a 10 nm diameter and a conformal Fe₃O₄ shell of 5 nm. It can be seen that the very broad weak shoulder at 760 nm in the rod-shaped particle spectrum is diminished in the presence of the LSPR contribution of the spherical particle peaked at 660 nm, leaving only one peak at 620 nm in the optical spectrum of the mixture. These simulated results thus explain the observation of only one peak in the optical spectrum of the core-shell structures when the shell is thick (Figure 3C). The peak at 590 nm mainly arises from the contributions of the transverse mode of the rod-shaped core-shell particles and the LSPR of the spherical core-shell particles. The discrepancy in the peak position is attributed to the size and shell thickness variations in the sample.

The metal-on-metal growth approach to the core-shell hybrid nanostructures can be extended to use other metal carbonyl complexes in the deposition process. We chose a less toxic metal carbonyl complex Mn₂(CO)₁₀ for the demonstration. To achieve the conformal deposition, the deposition procedure was carried out at 200 °C. Figure 5, A-C, displays the TEM results of the AuCu₃-MnO_x core-shell nanostructures consisting of 94% rod-shaped particles with an 8.9 × 21.1 nm core (diameter: 8.9±0.8 nm; length: 21.1±2.5 nm) and 6% spherical particles with a 10 nm core. The MnO_x shell is very thin, similar to that of the FeO_x shell, about 1-2 nm and largely amorphous, and it appears to be completely surrounding the AuCu₃ core as shown in the HRTEM and HADDF-STEM images. The shell seems to be slightly rougher than the FeO_x shell. The EDX mapping indicates the elemental distribution of a nanorod, confirming the AuCu₃-MnO_x core-shell structure. The UV-vis spectrum of the AuCu₃-MnO_x core-shell nanostructures exhibits the longitudinal mode of the LSPR at 710 nm and a shoulder peak at 560 nm (Figure 5D), similar to that of AuCu₃-FeO_x core-shell nanostructures with a thin shell of 1-2 nm.

In addition to the use of carbonyl complexes, we further extended the metal-on-metal growth

approach to other zero-valent metal-ligand complexes such as $\text{Ni}(\text{COD})_2$. The same deposition process at 200 °C was carried out by the use of $\text{Ni}(\text{COD})_2$ to replace $\text{Fe}(\text{CO})_5$ or $\text{Mn}_2(\text{CO})_{10}$. The resulting $\text{AuCu}_3\text{-NiO}_x$ core-shell structures were characterized by TEM (Figure 6A). Unlike FeO_x and MnO_x thin shells, the NiO_x shell tends to favorably deposit on the long side of the nanorods (Figure 6B). The incomplete coating is attributed to the relatively-low decomposition temperature of $\text{Ni}(\text{COD})_2$ at 60 °C under inert gas atmosphere⁴⁵ (vs. $T_{\text{decomp.}}$ of $\text{Fe}(\text{CO})_5$ at 80 °C and $\text{Mn}_2(\text{CO})_{10}$ 110 °C), leading to the increased amount of Ni atoms present to facilitate the island growth and thus thickening the shell to ~5 nm. Additionally, it was observed that the original AuCu_3 rod morphology was changed to more irregular shapes with decreased aspect ratios which were analyzed to be a mixture of 59% rod-shaped particles with a 10.0×20.0 nm core (diameter: 10.0 ± 1.5 nm; length: 20.0 ± 2.7 nm) and 41% spherical particles with a 10 nm core. From the EDX mapping, it appears that Au and Cu diffuse into the Ni shells and lead to the morphological reconstruction of the nanorods during the Ni deposition process (Figure 6C). This observation indicates the tendency of forming the solid solution of Cu-Au-Ni at the nanoscale at elevated temperatures. The UV-vis spectrum of the $\text{AuCu}_3\text{-NiO}_x$ core-shell nanostructures exhibits a peak at 600 nm corresponding to the transverse mode of the rod-shaped core-shell particles and the LSPR of the spherical core-shell particles (Figure 6D), similar to that of $\text{AuCu}_3\text{-FeO}_x$ core-shell nanostructures with a thick shell of 5 nm.

Upon the success in broadening the shell materials, we then looked into whether this metal-on-metal growth approach can be applied to pure Cu cores, which also exhibit LSPR in the visible region, but are more economical. The Cu cores with their surfaces passivated by TOP were synthesized using our previously-published method.²⁰ The Cu nanoparticles are mostly cubic in shape with an edge length of ~60 nm and exhibit a broad LSPR peak at ~640 nm (Figure S7). The

same deposition procedures for the thin oxide shells on the AuCu₃ nanorods were carried out to deposit Fe, Mn, and Ni on these Cu cores to yield Cu-FeO_x, Cu-MnO_x, and Cu-NiO_x core-shell structures, respectively. Mostly amorphous FeO_x and MnO_x thin shells (Figure 7, A-C, and D-F, respectively) were observed surrounding the Cu cores. The largely amorphous shells are also confirmed by XRD spectra of the core-shell structures which lack additional identifiable patterns other than the pattern of the face-centered cubic (fcc) Cu cores (Figure S8). The XPS analysis verifies that the presence of metal Cu cores and reveals that the valence state of Fe is Fe²⁺ and the valence state of Mn is dominated by a mixture of Mn(II), Mn(III), and Mn(IV) (Figure S9). These results are consistent with those on the AuCu₃ cores that reinforce one of the criteria of the metal-on-metal growth to form the conformal core-shell structures at the nanoscale – strain relaxation through the reduction of shell crystallinity. Similar to NiO_x on AuCu₃, an incomplete NiO_x shell was found on the Cu cores due to the relatively-low decomposition temperature of Ni(COD)₂ (Figure 7, G-I). The discontinuity of the NiO_x shell or the island growth of Ni on the Cu core is much more obvious than on the AuCu₃ core. This can be explained by the difference in bond dissociation energies which decrease in order of Au-Ni (247 kJ mol⁻¹) > Ni-Ni (204 kJ mol⁻¹) > Cu-Ni (201.7 kJ mol⁻¹).⁴⁶ In other words, the Au in the AuCu₃ alloy promotes the adhesion of Ni on its surface compared to pure Cu. In all cases, the LSPR of the core-shell structures is significantly damped and broadened compared to that of the Cu nanoparticles, as shown in Figure 7, J-K, for Cu-FeO_x, Cu-MnO_x, and Cu-NiO_x core-shell structures, respectively. Both the exotic oxide shells and the surface oxidation of Cu contribute to the severe damping for the LSPR of the Cu cores.^{20, 47}

We further applied a chemical method to etch the Cu cores by NH₄OH solution to generate hollow metal oxide structures. The resulting hollow structures can provide some insight to the

nanoscale metal-on-metal growth approach to the hybrid metal-metal oxide core-shell structures. Figure 8 displays the TEM results of these hollow metal oxide structures containing Fe and Mn, respectively. As expected, no hollow structures containing Ni were obtained due to the discontinuity of the NiO_x shell on the Cu cores. The thickness of these hollow shells is consistent with the shell thickness of the corresponding core-shell structures ~2 nm (Figure 8, A and D). Due to the poor crystallinity of the thin shells, no lattice fringes were observed in the HRTEM images of the hollow structures (Figure 8, B and E). However, it is surprising to find that these hollow structures also contain Cu, and the elements appear to homogeneously distribute across the hollow shells as shown in the EDX mapping (Figure 8, C and F). By analyzing the EDX spectra, there are Fe 85.92% and Cu 14.08% in the CuFeO_x hollow structures whereas the CuMnO_x hollow structures contain 38.48% Mn and 61.57% Cu (Figure S10). The EDX results are in close agreement with the ICP-MS analysis of the samples (71.61% Fe and 28.39% Cu in the CuFeO_x hollow structures; 25.58% Mn and 74.42% Cu in the CuMnO_x hollow structures). Compared to the core-shell structures, the XRD spectra of both the CuFeO_x and CuMnO_x hollow structures lack the peaks arisen from the fcc Cu, suggesting that the Cu cores have been completely dissolved during the etching process (Figure S11). The XPS analysis verifies that the presence of Cu(I) and Cu(II), and also reveals that the valence state of Fe is a mixture of Fe²⁺/ Fe³⁺ and the valence state of Mn is dominated by a mixture of Mn(II), Mn(III), and Mn(IV) (Figure S12). The presence of the mixed oxides in the hollow structures could be the result of interdiffusion between Cu and Fe/Mn during the metal-on-metal growth to the corresponding core-shell structures.⁴⁸⁻⁴⁹ It is implied that interdiffusion also plays a role in lowering the interfacial energy for the conformal deposition to the core-shell structures at the nanoscale. Additionally, one explanation for the CuMnO_x hollow structures having higher Cu content than the CuFeO_x hollow structures is that the

bond dissociation energy of Mn-Mn (61 kJ mol^{-1}) is lower than that of Fe-Fe (108 kJ mol^{-1}),⁴⁶ facilitating the interdiffusion during the Cu-MnO_x core-shell formation.

Figure 9 summarizes the metal-on-metal growth mechanism to core-shell structures of M-M'O_x (M = AuCu₃, Cu; M' = Fe, Mn, Ni). We look into some key factors for controlling the metal-on-metal growth in solution in order to achieve conformal deposition for the synthesis of hybrid core-shell structures. When deposition temperature is ramped from 110 to 200 °C at a rate of 2.5 °C/min, the thermal decomposition rate of the organometallic complexes increases in the order of Fe(CO)₅ < Mn₂(CO)₁₀ < Ni(COD)₂, resulting in a layer deposition of Fe and Mn on the seeds to form the conformal core-shell structures but an island growth of Ni on the seeds to generate incomplete core-shell structures. It is important to control the thermal decomposition of the metal zero-valent complexes during the deposition process. Choosing a reaction temperature close to the thermal decomposition temperature and slowing down the temperature ramp-up rate can effectively limit the concentration of the available atoms below the critical concentration of homogeneous nucleation, thus favoring heterogeneous growth. We successfully tested this hypothesis for the conformal deposition of the Ni shells by lowering the deposition temperature closer to the Ni(COD)₂ decomposition temperature. Figure 10A displays the Cu-NiO_x core-shell structure synthesized by ramping the temperature from 60 °C to 200 °C at the same rate (2.5 °C/min). Their corresponding CuNiO_x hollow structures showed in Figure 10B that verify the success of the NiO_x conformal deposition as a complete shell. The XRD spectra in Figure 10C confirm the amorphous nature of the NiO_x shells and the hollow structures. The XPS spectra in Figure 10D and Figure S13 indicate that Ni in the core-shell structures and the hollow structures exhibit a valence of 2+. The hollow CuNiO_x structures are made of 44.81% Cu and 55.19% Ni as analyzed by ICP-MS analysis. Compared to the core-shell structure, the surfaces of the hollow

structures were converted from oxides to hydroxides because of the NH_4OH treatment in the etching process. During the metal-on-metal growth, both the reduction of the strain energy (i.e. more amorphous shells) and the enhancement of the interdiffusion can facilitate the conformal deposition. Between these two mechanisms, we would argue that the former has a stronger influence as evidenced by the following two scenarios. The strain effect could introduce the island growth predominately between the two metals that can form solid solutions (e.g. Au and Cu).¹⁹ The amorphous shells (e.g. FeO_x) could be successfully coated on the dissimilar materials (e.g. Pd), but thermal annealing to increase crystallinity resulted in promoting the island formation of Pd- Fe_3O_4 heterostructures.¹⁵ Furthermore, the strength of the bond energy (ΔD_0) or bond dissociation energy ($\Delta D_0'$), which are slightly different by definition, but have the same trend,⁵⁰ can be applied to interpret the findings and thus form some guideline for predicting conformal deposition. When $\Delta D_0'$ of the two different metals (i.e. $\Delta D_0'_{\text{M-M}}$) is stronger than that of the metal the same (i.e. $\Delta D_0'_{\text{M-M}}$), it promotes the likelihood of conformal deposition.

Conclusion

We applied a metal-on-metal thin film growth approach to control the conformal deposition of nonprecious metal shells on the Cu-based metal cores to generate the hybrid metal-metal oxide core-shell structures. The deposition kinetics were controlled by a temperature-regulated thermal decomposition of zero-valent transition metal complexes. This approach was successfully demonstrated to synthesize $\text{AuCu}_3\text{-FeO}_x$ core-shell nanoparticles with a thin and a thick shell of ~ 2 nm and ~ 5 nm, respectively. The versatility of the approach was expanded to other metal oxides MnO_x and NiO_x and pure nonprecious metal Cu cores. The mechanisms of strain reduction and interdiffusion to promote conformal deposition over island growth were evidenced in the formation of these core-shell structures. The discrepancy of discontinuous NiO_x shell from

complete shells of FeO_x and MnO_x is attributed to low decomposition temperature of the $\text{Ni}(\text{COD})_2$ precursor and high Ni-Ni bond energy or bond dissociation energy. By lowering the initial deposition temperature, the conformal deposition of NiO_x shell was successfully achieved. This study provides some insightful guidance to the metal-on-metal growth in solution at the nanoscale for the synthesis of hybrid core-shell nanostructures. It is expected that the conformal deposition can be promoted by keeping the initial reaction temperature close to the thermal decomposition temperature of the zero-valent precursors.

These hybrid core-shell nanoparticles integrate the materials properties from both individual components. In some of these cases (e.g. $\text{AuCu}_3\text{-FeO}_x$), the core-shell nanoparticles exhibit both optical and magnetic properties. The plasmonic properties of the AuCu_3 cores in these core-shell structures were largely preserved while the Cu LSPR is damped more severely. The observed damping effects can be anticipated to progress proportionally with the increased thickness of the oxide shell. Despite damping effects, the plasmonic properties of these Cu-based core-metal oxide shell structures may have the potential to enable plasmon-enhanced applications such as photocatalysis, photothermal therapy, and photovoltaics.⁵¹ Involving nonprecious metal and metal oxides in these core-shell structures can further make these processes more economical. This chemical approach can be applicable to other core-shell structure syntheses.

SURPPORTING INFORMATION

XRD spectra of the AuCu₃-FeO_x core-shell structures; EDX spectral analysis of the thin shell AuCu₃-FeO_x core-shell structures; XPS spectra of the AuCu₃-FeO_x core-shell structures; DDA simulation of the AuCu₃ nanorods; the fitting of the LSPR peak position and optical efficiency as a function of the nanorod aspect ratio; the fitting of the LSPR peak position and optical efficiency as a function of the oxide shell thickness; TEM image and UV-vis spectrum of Cu nanoparticle cores; XRD spectra and XPS spectra of the Cu-MnO_x and Cu-MnO_x core-shell structures; EDX spectra, XRD spectra and XPS spectra of the CuFeO_x and CuMnO_x hollow structures; and XPS spectra of the Cu-NiO_x core-shell structures and the CuNiO_x hollow structures.

ACKNOWLEDGEMENT

This work was in part funded by the Arkansas Breast Cancer Research Program, Arkansas Bioscience Institute, Women's Giving Circle at the University of Arkansas, and the grant NSF CBET 1703827. We would like to thank the support for the infrastructure by the grant NSF EPSCoR OIA 1457888. The microscopic work done at Brookhaven National Laboratory is sponsored by the U.S. DOE BES, by the Materials Sciences and Engineering Division, and Early Career Research Program under Contract DE-SC0012704. ICP-MS measurements were carried out at the Arkansas Mass Spectrometry Facility, which is supported by the Arkansas Biosciences Institute.

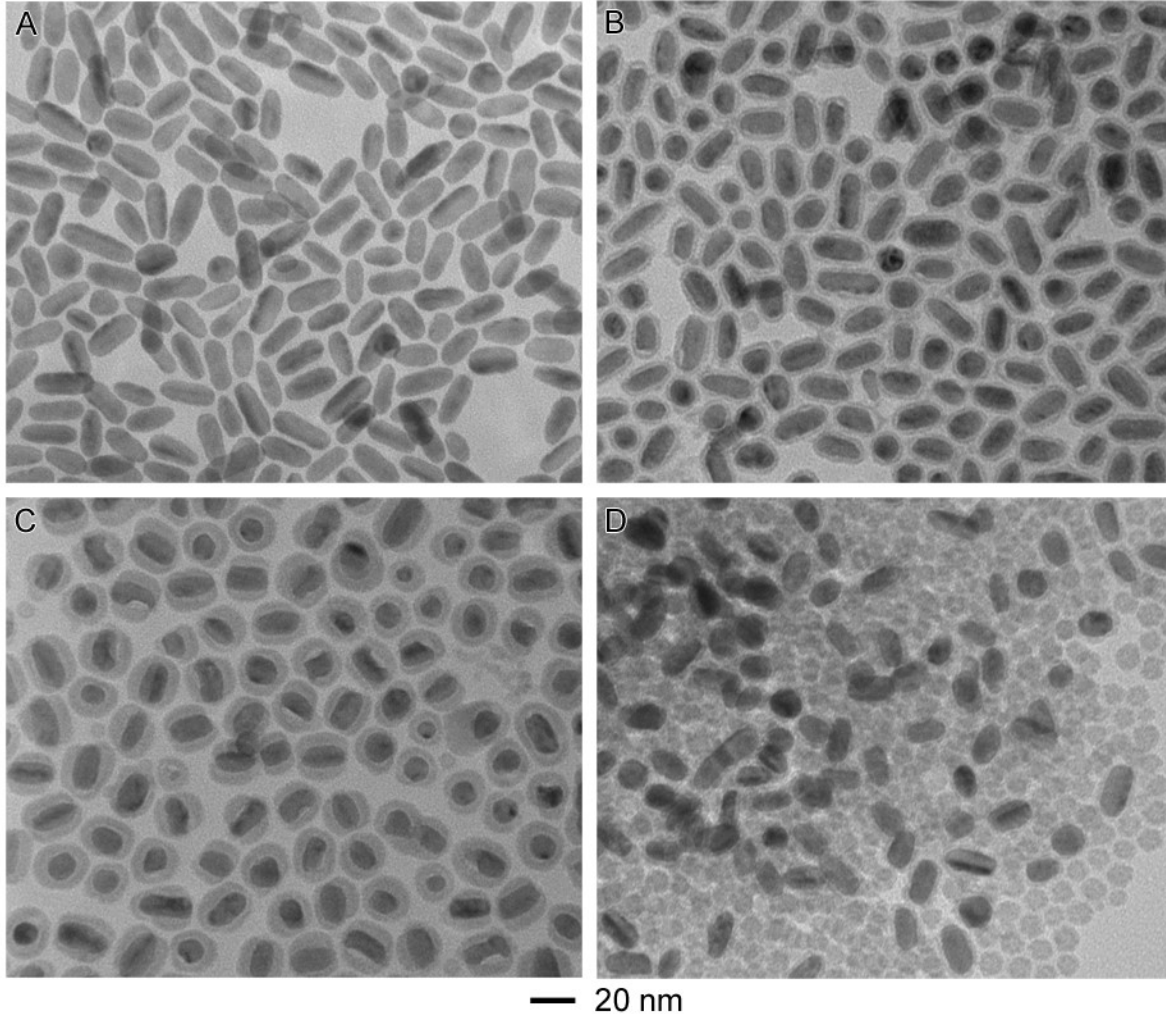


Figure 1. TEM images of the temperature-controlled deposition of the FeO_x shells on the AuCu_3 nanostructures: (A) AuCu_3 nanostructures containing 94% nanorods with an aspect ratio of 9.6×21.3 nm and 6% spherical nanoparticles with a diameter of 10 nm; (B) $\text{AuCu}_3\text{-FeO}_x$ core-shell structures with a thin shell of 1-2 nm prepared at 200 °C containing 78% rod-shaped particles with a 9.0×20.4 nm core and 22% spherical particles with a 10 nm core; (C) $\text{AuCu}_3\text{-FeO}_x$ core-shell structures a thick shell of 5-6 nm prepared at 280 °C containing 48% rod-shaped particles with a 9.6×18.3 nm core and 52% spherical particles with a 10 nm core; and (D) a mixture of $\text{AuCu}_3\text{-FeO}_x$ core-shell structures and free iron oxide particles prepared at 315 °C.

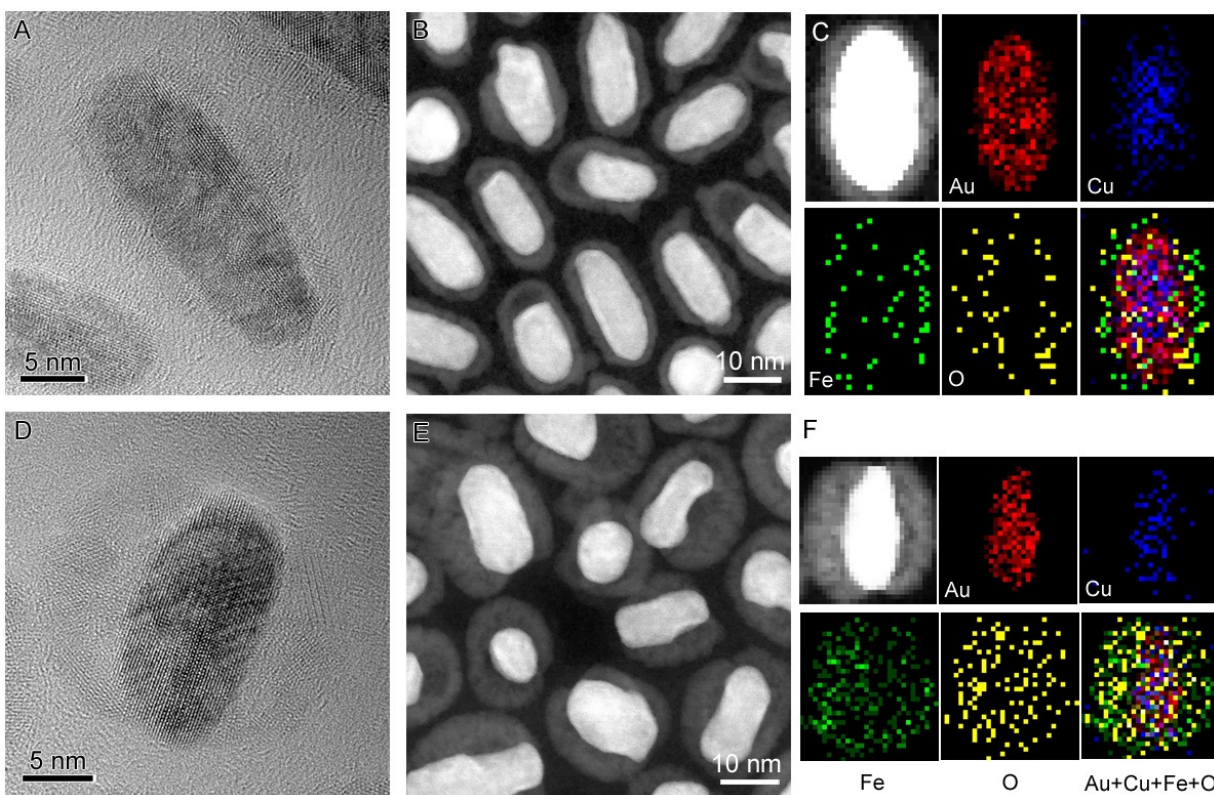


Figure 2. TEM characterization of the $\text{AuCu}_3\text{-FeO}_x$ core-shell nanostructures with a thin shell of 2 nm: (A) HRTEM; (B) HAADF-STEM; and (C) EDX elemental mapping; and with a thick shell of 5 nm: (D) HRTEM; (E) HAADF-STEM; and (F) EDX elemental mapping.

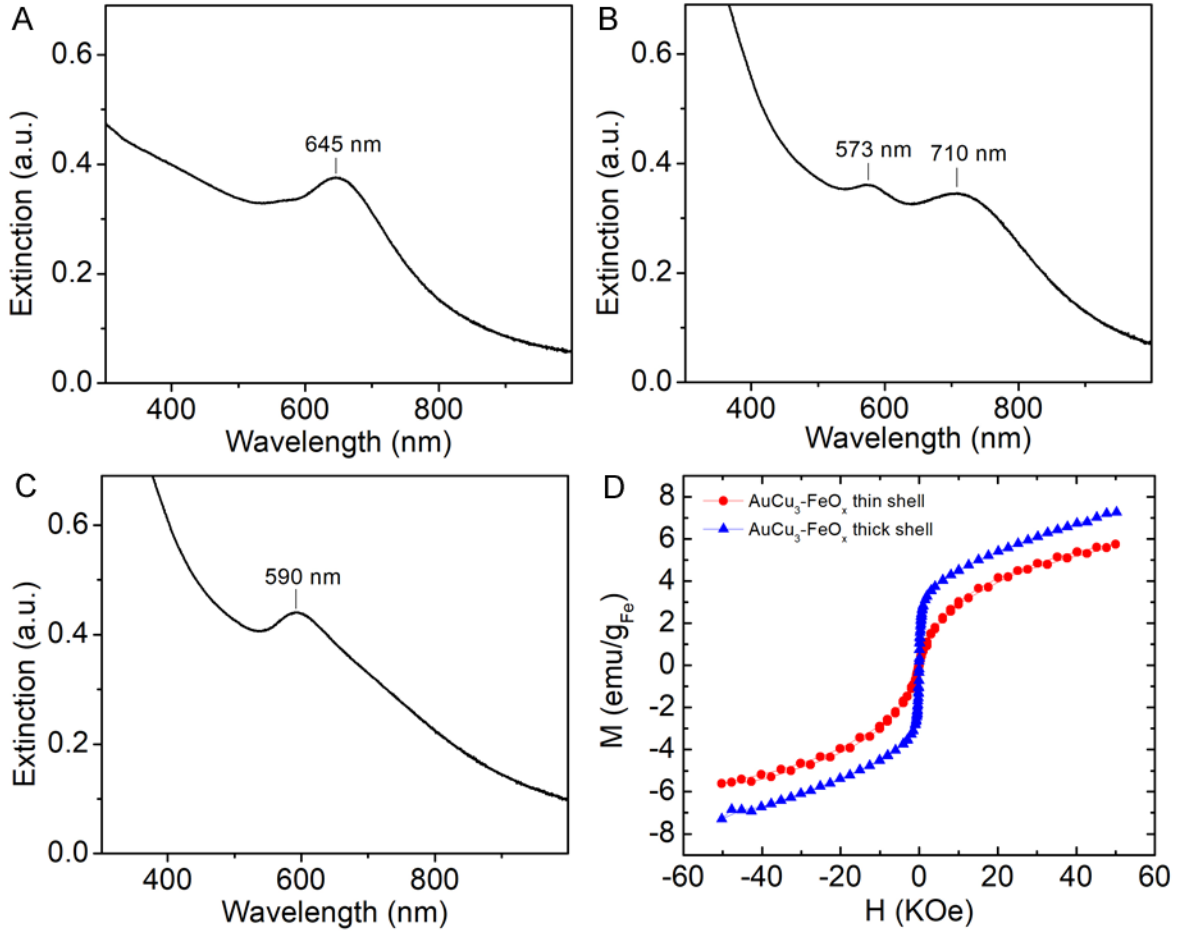


Figure 3. (A-C) UV-vis spectra of the corresponding samples (A-C) in Figure 1: (A) AuCu₃ nanostructures containing 94% nanorods with an aspect ratio of 9.6×21.3 nm and 6% spherical nanoparticles with a diameter of ~ 10 nm; (B) AuCu₃-FeO_x core-shell structures with a thin shell of 1-2 nm prepared at 200 °C containing 78% rod-shaped particles with a 9.0×20.4 nm core and 22% spherical particles with a 10 nm core; (C) AuCu₃-FeO_x core-shell structures a thick shell of 5-6 nm prepared at 280 °C containing 48% rod-shaped particles with a 9.6×18.3 nm core and 52% spherical particles with a 10 nm core. (D) Magnetic measurements of the AuCu₃-FeO_x core-shell structures coated with a FeO_x thin shell (red) and a thick shell (blue).

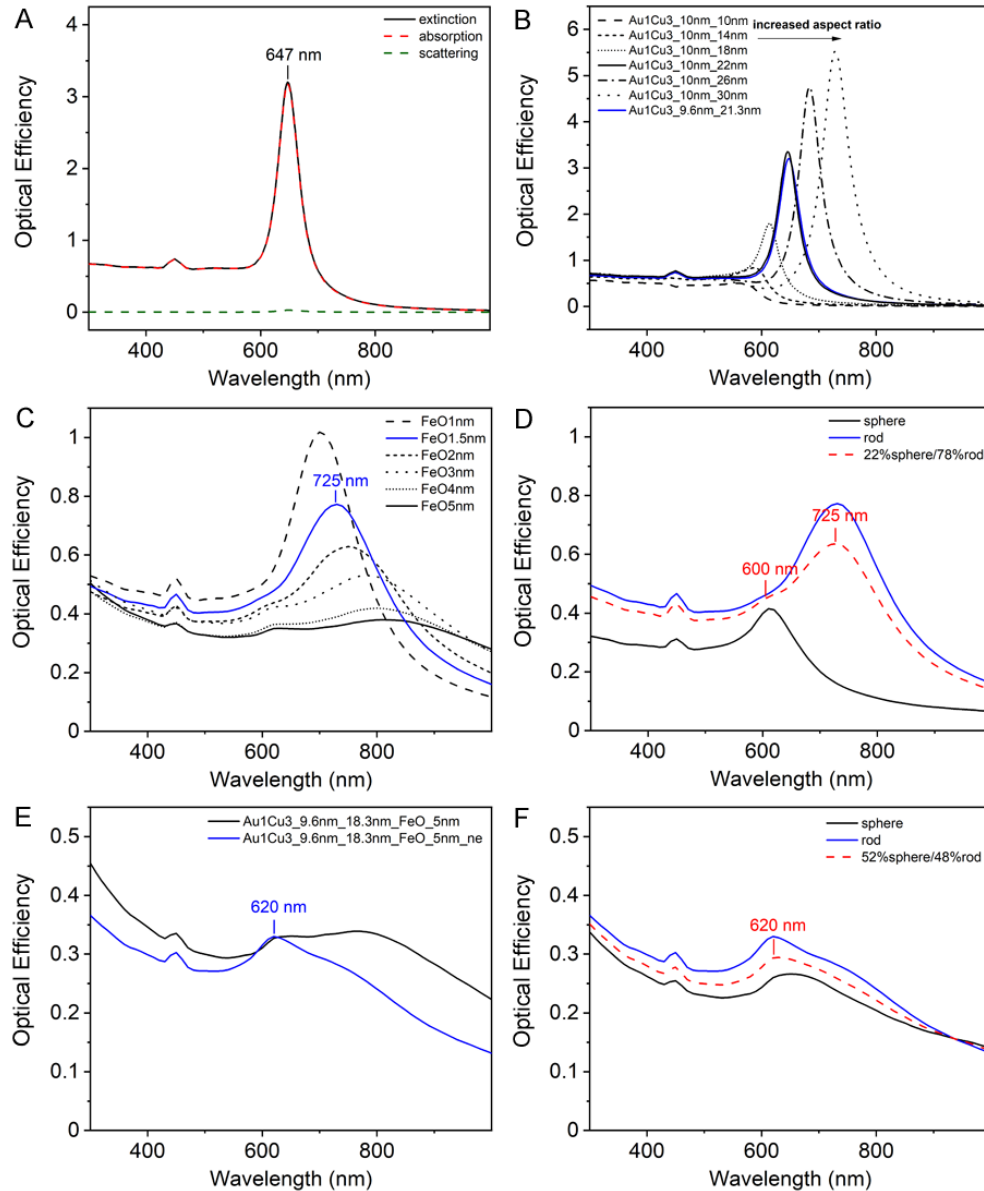


Figure 4. DDA simulation of the optical spectra of the nanostructures with different configurations: (A) extinction, absorption, scattering spectra of the AuCu₃ nanorods with an aspect ratio of 9.6×21.3 nm; (B) extinction spectra of a set of AuCu₃ nanorods with a diameter of 10 nm but increased lengths (for comparison the extinction spectrum of (A) is also plotted and colored in blue); (C) extinction spectra of the AuCu₃ nanorods (an aspect ratio of 9.6×21.3 nm) coated with conformal Fe₃O₄ layers of different thickness (spectrum in blue corresponding to the AuCu₃ nanorod coating with a 1.5 nm Fe₃O₄ shell); (D) linear combination spectrum (red dash) of extinction spectrum of 10 nm spheres coated with a 1.5 nm Fe₃O₄ shell (black, 22%) and 9.6×21.3 nm rods coated with a 1.5 nm Fe₃O₄ shell (blue, 78%); (E) extinction spectra of the AuCu₃ nanorods (an aspect ratio of 9.6×18.3 nm) coated with either a conformal Fe₃O₄ layer of 5 nm (black) or an incomplete layer of 5 nm only deposited on the long side of the rod (blue); (F) linear combination spectrum (red dash) of extinction spectrum of 10 nm spheres coated with a 5 nm Fe₃O₄ shell (52%, black) and 9.6×18.3 nm rods coated with a 5 nm Fe₃O₄ shell (48%, blue).

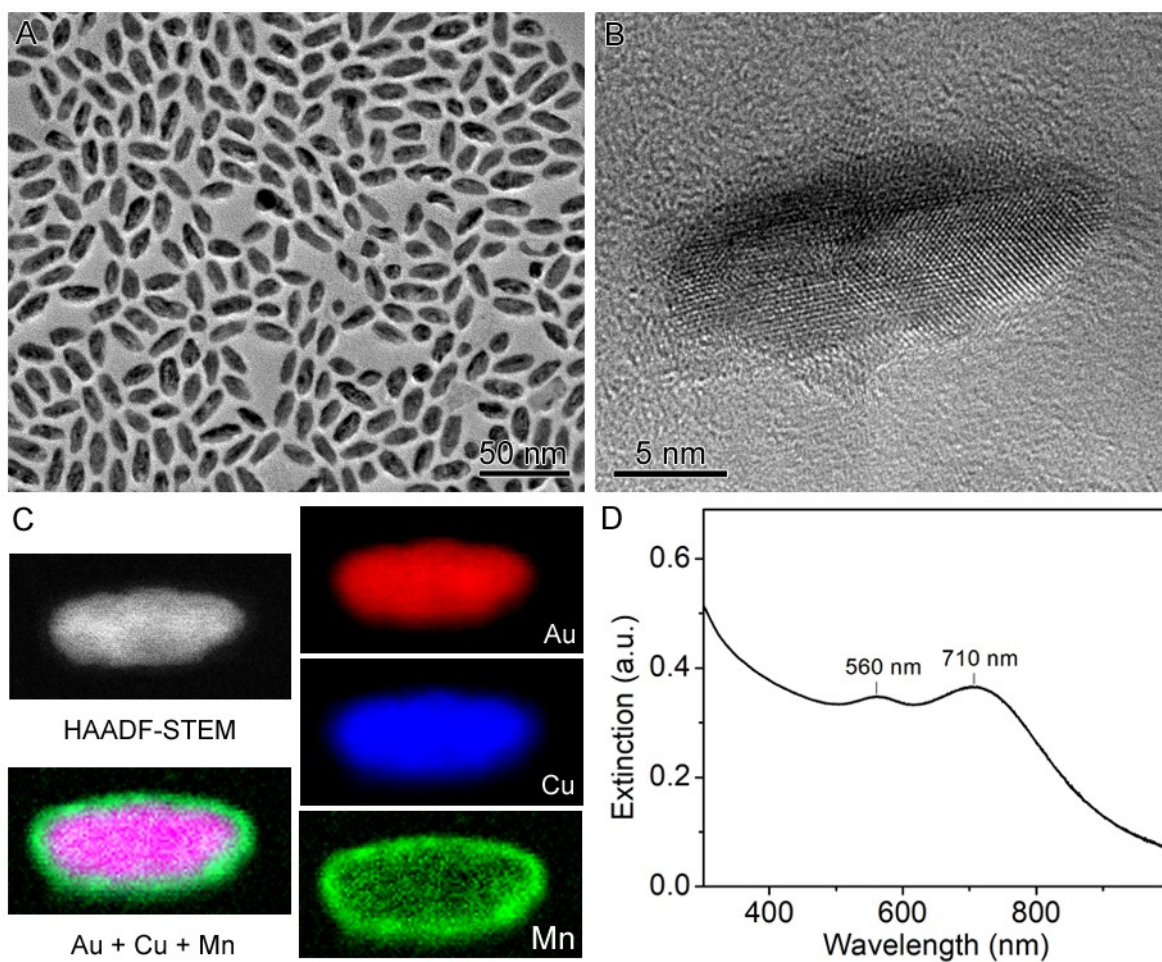


Figure 5. (A-C) TEM characterization of the $\text{AuCu}_3\text{-MnO}_x$ core-shell nanostructures: (A) TEM image showing that the $\text{AuCu}_3\text{-MnO}_x$ core-shell structures prepared at 200 °C containing 94% rod-shaped particles with a 8.9×21.1 nm core and 6% spherical particles with a 10 nm core; (B) HRTEM image indicating a core-shell structure; (C) HAADF-STEM image and EDX mapping indicating the elemental distribution of a Au-Cu-containing core and a Mn-containing shell. (D) UV-vis spectrum of the $\text{AuCu}_3\text{-MnO}_x$ core-shell nanostructures suspended in toluene.

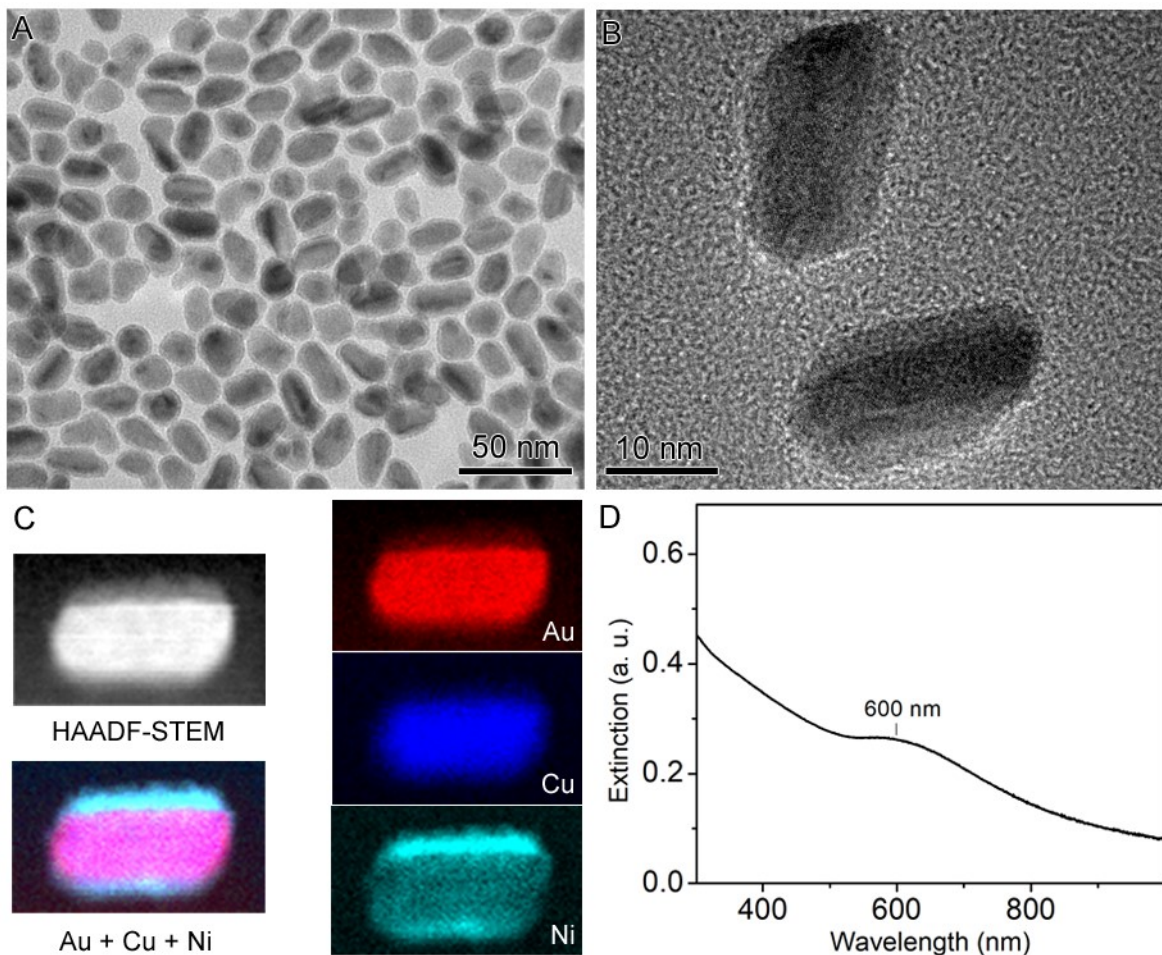


Figure 6. TEM characterization of the $\text{AuCu}_3\text{-NiO}_x$ core-shell nanostructures: (A) TEM image showing that $\text{AuCu}_3\text{-NiO}_x$ core-shell structures prepared at 200 °C containing 59% rod-shaped particles with a 10.0× 20.0 nm core and 41% spherical particles with a 10 nm core; (B) HRTEM image indicating an incomplete core-shell structure; (C) HAADF-STEM image and EDX mapping indicating the elemental distribution of a Au-Cu-containing core and an unevenly-coated, Ni-containing shell. (D) UV-vis spectrum of the $\text{AuCu}_3\text{-NiO}_x$ core-shell nanostructures suspended in toluene.

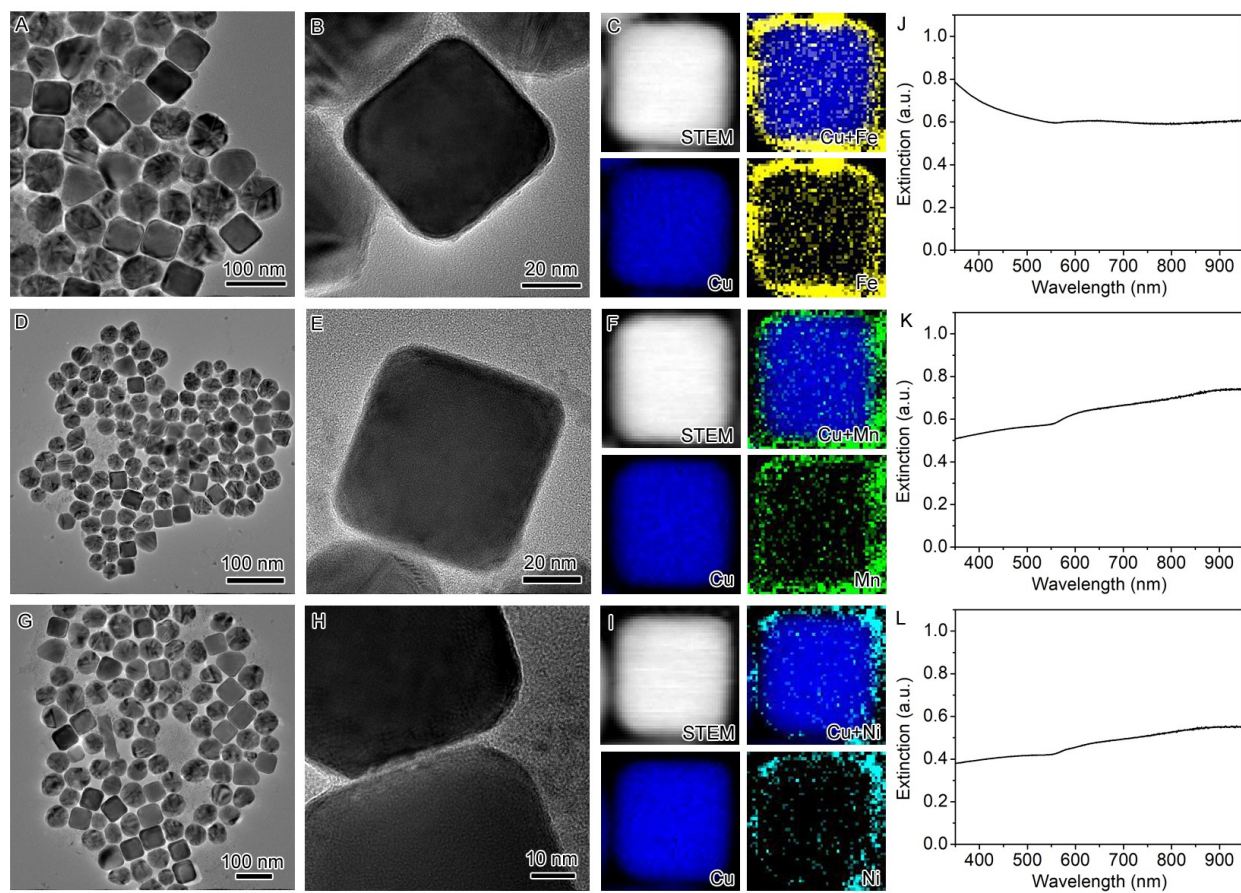


Figure 7. (A-C) TEM characterization of the Cu-FeO_x core-shell nanostructures: (A) TEM image; (B) HRTEM; (C) HAADF-STEM image and EDX elemental mapping. (D-F) TEM characterization of Cu-MnO_x core-shell nanostructures: (D) TEM image; (E) HRTEM; (F) HAADF-STEM image and EDX elemental mapping. (G-I) TEM characterization of Cu-NiO_x core-shell nanostructures: (G) TEM image; (H) HRTEM image; (I) HAADF-STEM image and EDX elemental mapping. (J-L) UV-vis spectra of the corresponding core-shell samples suspended in toluene: (J) Cu-FeO_x; (K) Cu-MnO_x; and (L) Cu-NiO_x.

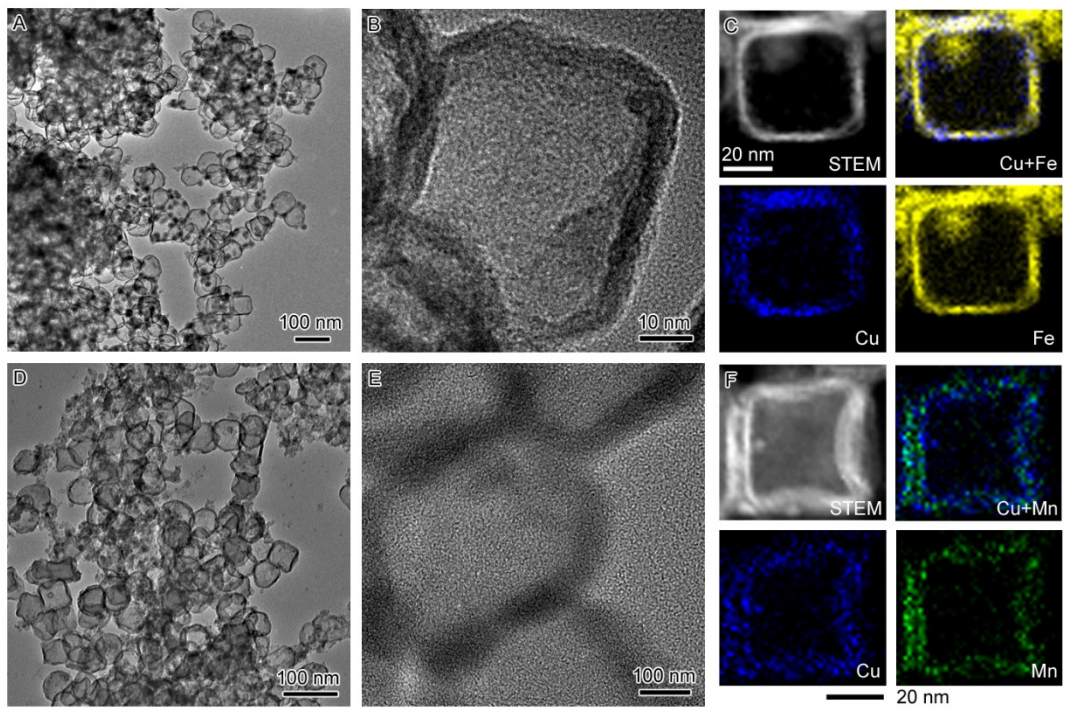


Figure 8. TEM characterization of CuMO_x hollow shells: (A-C) TEM, HRTEM, and STEM/EDX mapping of CuFeO_x ; and (D-F) TEM, HRTEM, and STEM/EDX mapping of CuMnO_x .

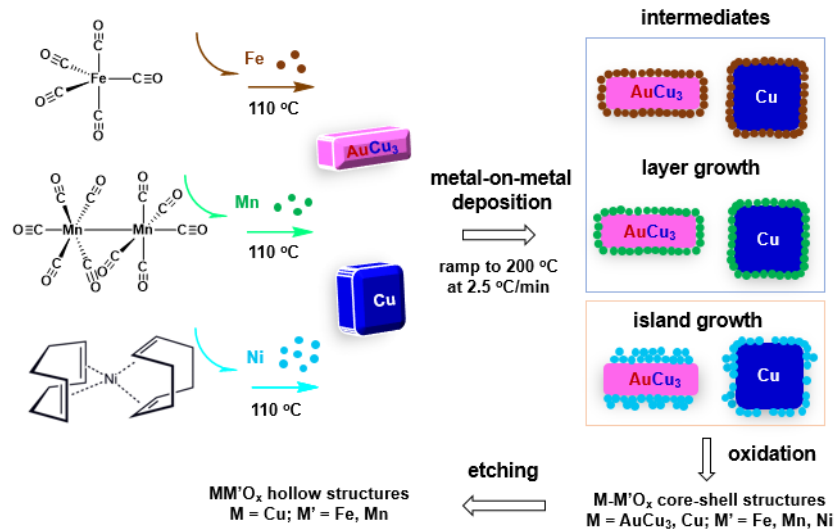


Figure 9. Schematic illustration of the metal-on-metal growth mechanism to core-shell structures of $\text{M-M}'\text{O}_x$ ($\text{M} = \text{AuCu}_3, \text{Cu}$; $\text{M}' = \text{Fe, Mn, Ni}$). When deposition temperature is ramped from 110 to $200\text{ }^\circ\text{C}$ at a rate of $2.5\text{ }^\circ\text{C}/\text{min}$, the thermal decomposition rate of the organometallic complexes increases in the order of $\text{Fe}(\text{CO})_5 < \text{Mn}_2(\text{CO})_{10} < \text{Ni}(\text{COD})_2$, resulting in a layer deposition of Fe and Mn on the seeds to form the conformal core-shell structures but an island growth of Ni on the seeds to generate incomplete core-shell structures. The Cu cores can be chemically etched by NH_4OH solution to generate $\text{MM}'\text{O}_x$ hollow structures ($\text{M} = \text{Cu}$; $\text{M}' = \text{Fe, Mn}$).

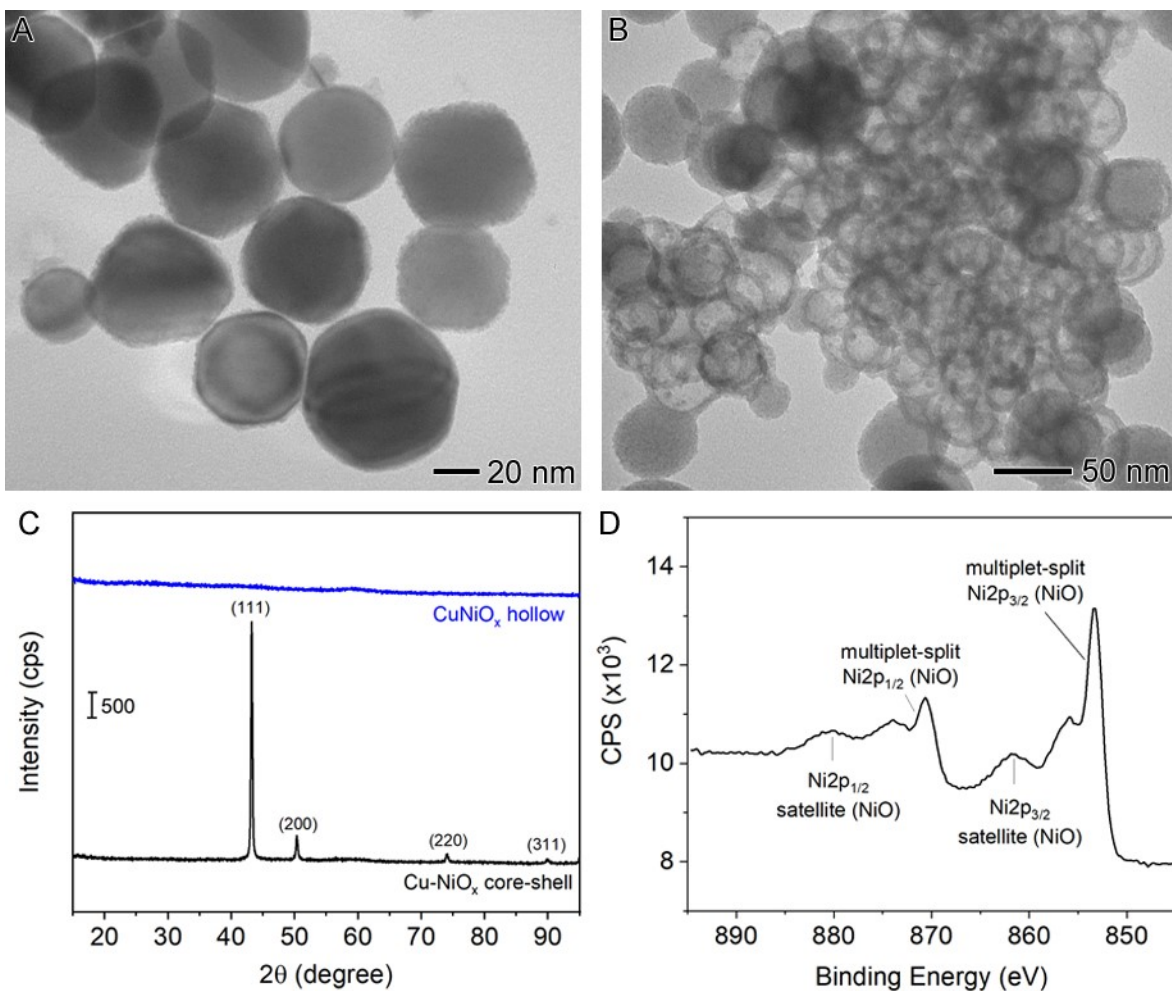


Figure 10. (A) TEM image of the Cu-NiO_x core-shell structures synthesized by lowering the deposition temperature to 60 °C; (B) TEM image of the CuNiO_x hollow shells obtained from chemical etching of the sample in (A) using NH₄OH; (C) XRD spectra of the Cu-NiO_x core-shell structures (black curve) and the CuNiO_x hollow shells (blue curve); and (D) XPS spectrum of the Ni in the Cu-NiO_x core-shell structures indicating that the valence of Ni is 2+.

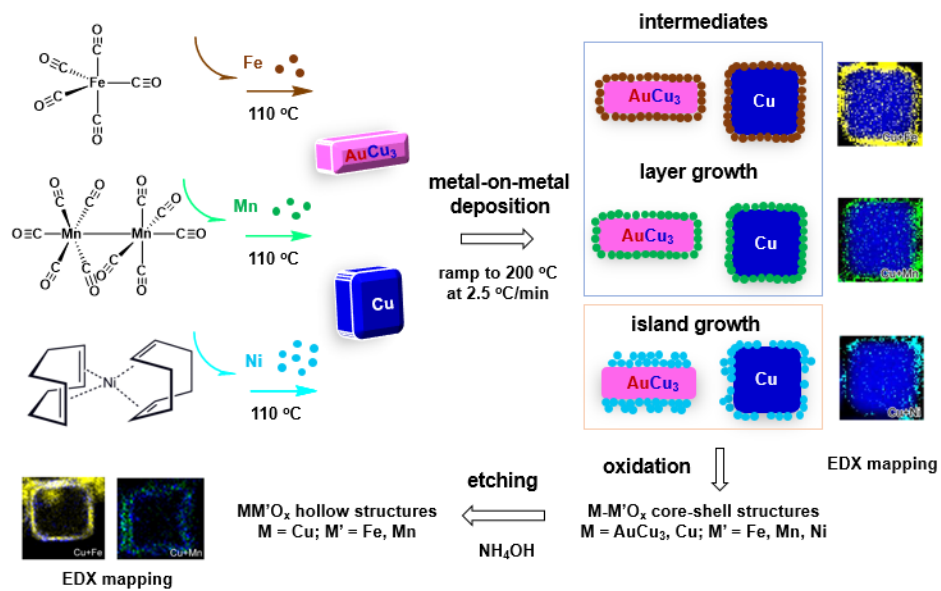
REFERENCES

1. Adams, D. M.; Brus, L.; Chidsey, C. E. D.; Creager, S.; Creutz, C.; Kagan, C. R.; Kamat, P. V.; Lieberman, M.; Lindsay, S.; Marcus, R. A., et al., Charge Transfer on the Nanoscale: Current Status. *J. Phys. Chem. B* **2003**, *107*, 6668-6697.
2. Linic, S.; Christopher, P.; Ingram, D. B., Plasmonic-Metal Nanostructures for Efficient Conversion of Solar to Chemical Energy. *Nat. Mater.* **2011**, *10*, 911.
3. Gao, J.; Gu, H.; Xu, B., Multifunctional Magnetic Nanoparticles: Design, Synthesis, and Biomedical Applications. *Acc. Chem. Res.* **2009**, *42*, 1097-1107.
4. Hao, R.; Xing, R.; Xu, Z.; Hou, Y.; Gao, S.; Sun, S., Synthesis, Functionalization, and Biomedical Applications of Multifunctional Magnetic Nanoparticles. *Adv. Mater.* **2010**, *22*, 2729-2742.
5. Armelles, G.; Cebollada, A.; García-Martín, A.; González, M. U., Magnetoplasmonics: Combining Magnetic and Plasmonic Functionalities. *Adv. Opt. Mater.* **2013**, *1*, 10-35.
6. Zhu, Y.; Stubbs, L. P.; Ho, F.; Liu, R.; Ship, C. P.; Maguire, J. A.; Hosmane, N. S., Magnetic Nanocomposites: A New Perspective in Catalysis. *ChemCatChem* **2010**, *2*, 365-374.
7. Rossi, L. M.; Costa, N. J.; Silva, F. P.; Wojcieszak, R., Magnetic Nanomaterials in Catalysis: Advanced Catalysts for Magnetic Separation and Beyond. *Green Chem.* **2014**, *16*, 2906-2933.
8. Cortie, M. B.; McDonagh, A. M., Synthesis and Optical Properties of Hybrid and Alloy Plasmonic Nanoparticles. *Chem. Rev.* **2011**, *111*, 3713-3735.
9. Bigall, N. C.; Parak, W. J.; Dorfs, D., Fluorescent, Magnetic and Plasmonic—Hybrid Multifunctional Colloidal Nano Objects. *Nano Today* **2012**, *7*, 282-296.
10. Yu, H.; Chen, M.; Rice, P. M.; Wang, S. X.; White, R.; Sun, S., Dumbbell-Like Bifunctional Au–Fe₃O₄ Nanoparticles. *Nano Lett.* **2005**, *5*, 379-382.
11. Wang, C.; Daimon, H.; Sun, S., Dumbbell-Like Pt–Fe₃O₄ Nanoparticles and Their Enhanced Catalysis for Oxygen Reduction Reaction. *Nano letters* **2009**, *9*, 1493-1496.
12. Najafshirvari, S.; Kokumai, T. M.; Marras, S.; Destro, P.; Prato, M.; Scarpellini, A; Brescia, R.; Lak, A.; Pellegrino, T.; Zanchet, D., et al., Dumbbell-Like Au_{0.5}Cu_{0.5}@Fe₃O₄ Nanocrystals: Synthesis, Characterization, and Catalytic Activity in CO Oxidation. *ACS Appl. Mater. Interfaces* **2016**, *8*, 28624-28632.
13. Teng, X.; Black, D.; Watkins, N. J.; Gao, Y.; Yang, H., Platinum-Maghemite Core–Shell Nanoparticles Using a Sequential Synthesis. *Nano Lett.* **2003**, *3*, 261-264.
14. Fantechi, E.; Roca, A. G.; Sepúlveda, B.; Torruella, P.; Estradé, S.; Peiró, F.; Coy, E.; Jurga, S.; Bastús, N. G.; Nogués, J., Seeded Growth Synthesis of Au–Fe₃O₄ Heterostructured Nanocrystals: Rational Design and Mechanistic Insights. *Chem. Mater.* **2017**, *29*, 4022-4035.
15. Chen, S.; Si, R.; Taylor, E.; Janzen, J.; Chen, J., Synthesis of Pd/Fe₃O₄ Hybrid Nanocatalysts with Controllable Interface and Enhanced Catalytic Activities for CO Oxidation. *J. Phys. Chem. C* **2012**, *116*, 12969-12976.
16. Jiang, M.; Liu, W.; Yang, X.; Jiang, Z.; Yao, T.; Wei, S.; Peng, X., Pt/Fe₃O₄ Core/Shell Triangular Nanoprisms by Heteroepitaxy: Facet Selectivity at the Pt–Fe₃O₄ Interface and the Fe₃O₄ Outer Surface. *ACS Nano* **2015**, *9*, 10950-10960.
17. Klunker, M.; Nawaz Tahir, M.; Ragg, R.; Korschelt, K.; Simon, P.; Gorelik, T. E.; Barton, B.; Shylin, S. I.; Panthöfer, M.; Herzberger, J., Pd@Fe₂O₃ Superparticles with Enhanced Peroxidase Activity by Solution Phase Epitaxial Growth. *Chem. Mater.* **2017**, *29*, 1134-1146.
18. Steimle, B. C.; Fenton, J. L.; Schaak, R. E., Rational Construction of a Scalable Heterostructured Nanorod Megalibrary. *Science* **2020**, *367*, 418-424.

19. Chen, S.; Jenkins, S. V.; Tao, J.; Zhu, Y.; Chen, J., Anisotropic Seeded Growth of Cu–M (M = Au, Pt, or Pd) Bimetallic Nanorods with Tunable Optical and Catalytic Properties. *J. Phys. Chem. C* **2013**, *117*, 8924-8932.
20. Crane, C. C.; Wang, F.; Li, J.; Tao, J.; Zhu, Y.; Chen, J., Synthesis of Copper–Silica Core–Shell Nanostructures with Sharp and Stable Localized Surface Plasmon Resonance. *J. Phys. Chem. C* **2017**, *121*, 5684-5692.
21. Draine, B. T.; Flatau, P. J., Discrete-Dipole Approximation for Periodic Targets: Theory and Tests. *J. Opt. Soc. Am. A* **2008**, *25*, 2693-2703.
22. Draine, B. T.; Flatau, P. J., User Guide for the Discrete Dipole Approximation Code DDSCAT 7.3. *arXiv preprint arXiv:1305.6497* **2013**.
23. Johnson, P. B.; Christy, R.-W., Optical Constants of the Noble Metals. *Phys. Rev. B* **1972**, *6*, 4370.
24. Schlegel, A.; Alvarado, S.; Wachter, P., Optical Properties of Magnetite Fe₃O₄. *J. Phys. C: Solid State Phys.* **1979**, *12*, 1157.
25. Dewar, J.; Jones, H. O., The Physical and Chemical Properties of Iron Carbonyl. *Proceedings of the Royal Society of London. Series A, Containing Papers of a Mathematical and Physical Character* **1905**, *76*, 558-577.
26. Pescia, D.; Stampanoni, M.; Bona, G. L.; Vaterlaus, A.; Willis, R. F.; Meier, F., Magnetism of Epitaxial Fcc Iron Films on Cu(001) Investigated by Spin-Polarized Photoelectron Emission. *Phys. Rev. Lett.* **1987**, *58*, 2126-2129.
27. Steigerwald, D. A.; Egelhoff, J. W. F., Epitaxial Fcc Fe Films on Cu(100). *Phys. Rev. Lett.* **1988**, *60*, 2558-2558.
28. Cao, Y.; Montano, P. A., High Resolution Leed Study of the Fe Growth Mode on Cu (100), Cu (110) and Cu (111) Surfaces. *Interface Dynamics and Growth* **1991**, *237*, 435-440.
29. Detzel, T.; Memmel, N., Substrate Diffusion in Metastable Ultrathin Films: Iron on Cu(001). *Phys. Rev. B* **1994**, *49*, 5599-5606.
30. Hothersall, D. C., Crystallographic and Magnetic Properties of Thin Films of Iron Epitaxially Grown on F.C.C. Substrates. *Phil. Mag.* **1967**, *15*, 1023-1033.
31. Lu, S. H.; Quinn, J.; Tian, D.; Jona, F.; Marcus, P. M., Structural Properties of Epitaxial Films of Fe on Cu and Cu-Based Surface and Bulk Alloys. *Surf. Sci.* **1989**, *209*, 364-378.
32. Macedo, W. A. A.; Keune, W.; Ellerbrock, E. D., Magnetic Properties of Ultrathin Epitaxial Fcc-Fe(001) Films on Cu(001) and Cu₃Au(001). *J. Magn. Magn. Mater.* **1991**, *93*, 552-556.
33. Baudalet, F.; Lin, M. T.; Kuch, W.; Meinel, K.; Choi, B.; Schneider, C. M.; Kirschner, J., Perpendicular Anisotropy and Spin Reorientation in Epitaxial Fe/Cu₃Au(100) Thin Films. *Phys. Rev. B* **1995**, *51*, 12563-12578.
34. Lin, M. T.; Shen, J.; Kuch, W.; Jenniches, H.; Klaua, M.; Schneider, C. M.; Kirschner, J., Structural Transformation and Spin-Reorientation Transition in Epitaxial Fe/Cu₃Au(100) Ultrathin Films. *Phys. Rev. B* **1997**, *55*, 5886-5897.
35. Schirmer, B.; Feldmann, B.; Wuttig, M., Limits of Metastable Epitaxy: The Structure of Ultrathin Fe Films on Cu₃Au (100). *Phys. Rev. B* **1998**, *58*, 4984-4991.
36. Bauer, E., Phänomenologische Theorie Der Kristallabscheidung an Oberflächen. I. *Z. Krist.-Cryst. Mater.* **1958**, *110*, 372-394.
37. Lopes, G.; Vargas, J. M.; Sharma, S. K.; Béron, F.; Pirota, K. R.; Knobel, M.; Rettori, C.; Zysler, R. D., Ag–Fe₃O₄ Dimer Colloidal Nanoparticles: Synthesis and Enhancement of Magnetic Properties. *J. Phys. Chem. C* **2010**, *114*, 10148-10152.

38. Brollo, M. E. F.; López-Ruiz, R.; Muraca, D.; Figueroa, S. J. A.; Pirota, K. R.; Knobel, M., Compact Ag@Fe₃O₄ Core-Shell Nanoparticles by Means of Single-Step Thermal Decomposition Reaction. *Sci. Rep.* **2014**, *4*, 6839.
39. Mourdikoudis, S.; Liz-Marzán, L. M., Oleylamine in Nanoparticle Synthesis. *Chem. Mater.* **2013**, *25*, 1465-1476.
40. Yin, Y.; Rioux, R. M.; Erdonmez, C. K.; Hughes, S.; Somorjai, G. A.; Alivisatos, A. P., Formation of Hollow Nanocrystals through the Nanoscale Kirkendall Effect. *Science* **2004**, *304*, 711-714.
41. Peng, S.; Sun, S., Synthesis and Characterization of Monodisperse Hollow Fe₃O₄ Nanoparticles. *Angew. Chem. Int. Ed.* **2007**, *46*, 4155-4158.
42. Phu, N. D.; Ngo, D. T.; Hoang, L. H.; Luong, N. H.; Chau, N.; Hai, N. H., Crystallization Process and Magnetic Properties of Amorphous Iron Oxide Nanoparticles. *J. Phys. D: Appl. Phys.* **2011**, *44*, 345002.
43. Kelly, K. L.; Coronado, E.; Zhao, L. L.; Schatz, G. C., The Optical Properties of Metal Nanoparticles: The Influence of Size, Shape, and Dielectric Environment. *J. Chem. Phys. B* **2003**, *107*, 668-677.
44. Henry, A.-I.; Bingham, J. M.; Ringe, E.; Marks, L. D.; Schatz, G. C.; Van Duyne, R. P., Correlated Structure and Optical Property Studies of Plasmonic Nanoparticles. *J. Phys. Chem. C* **2011**, *115*, 9291-9305.
45. Schunn, R.A., Ittel, S.D., Cushing, M.A., Baker, R., Gilbert, R.J. and Madden, D.P., 1990. Bis (1, 5-Cyclooctadiene) Nickel (0). *Inorganic Syntheses: Reagents for Transition Metal Complex and Organometallic Syntheses*, *28*, pp.94-98.
46. Luo, Y.-R., *Comprehensive Handbook of Chemical Bond Energies*; CRC press, 2007.
47. Chan, G. H.; Zhao, J.; Hicks, E. M.; Schatz, G. C.; Van Duyne, R. P., Plasmonic Properties of Copper Nanoparticles Fabricated by Nanosphere Lithography. *Nano Lett.* **2007**, *7*, 1947-1952.
48. Butrymowicz, D. B.; Manning, J. R.; Read, M. E., Diffusion in Copper and Copper Alloys Part IV. Diffusion in Systems Involving Elements of Group VIII. *J. Phys. Chem. Ref. Data* **1976**, *5*, 103-200.
49. Iijima, Y.; Hirano, K.-i.; Sato, K., Interdiffusion in Cu–Mn Alloys. *Trans. Jpn Inst. Met.* **1977**, *18*, 835-842.
50. King, R.B., **2006**. Bond Energies. *Encyclopedia of Inorganic Chemistry*, pp.1-4.
51. Zhou, N.; López-Puente, V.; Wang, Q.; Polavarapu, L.; Pastoriza-Santos, I.; Xu, Q.-H., Plasmon-Enhanced Light Harvesting: Applications in Enhanced Photocatalysis, Photodynamic Therapy and Photovoltaics. *RSC Adv.* **2015**, *5*, 29076-29097.

Table of Contents



Keywords: AuCu₃ nanorods, Cu nanoparticles, iron oxide, manganese oxide, nickel oxide